Applied Catalysis B: Environmental 342 (2024) 123407

Contents lists available at ScienceDirect

Applied Catalysis B: Environmental

journal homepage: www.elsevier.com/locate/apcatb

Modulating Fe spin state in FeNC catalysts by adjacent Fe atomic clusters to facilitate oxygen reduction reaction in proton exchange membrane fuel cell

Chengjie Chen [a,1], Yinlong Wu [a,1], Xiulan Li [a], Yanting Ye [a], Zilong Li [a], Yifan Zhou [b], Jian Chen [b], Muzi Yang [b], Fangyan Xie [b], Yanshuo Jin [a], Colton Jones [c], Nan Wang [a,*], Hui Meng [a,*], Shaowei Chen [c,*]

[a] Guangdong Provincial Key Laboratory of Optical Fiber Sensing and Communications, Siyuan laboratory, Guangzhou Key Laboratory of Vacuum Coating Technologies and New Energy Materials, Guangdong Provincial Engineering Technology Research Center of Vacuum Coating Technologies and New Energy Materials, Department of Physics, Jinan University, Guangzhou, Guangdong 510632, China
[b] Instrumental Analysis & Research Center, Sun Yat-sen University, Guangzhou, Guangdong 510275, China
[c] Department of Chemistry and Biochemistry, University of California, 1156 High Street, Santa Cruz, CA 95064, United States

ARTICLE INFO

Keywords:
Single atom site
Few-atom cluster
Spin state
Oxygen reduction reaction
Proton exchange membrane fuel cell

ABSTRACT

Iron,nitrogen-codoped carbon (FeNC) has emerged as promising alternatives to precious metals for oxygen reduction reaction (ORR). Herein, we demonstrate that the ORR activity of FeNC can be markedly enhanced by the incorporation of adjacent Fe few-atom clusters (Fe_{AC}), where the octahedral field of Fe_{AC} boosts the splitting of the parallelogram field of FeN_4, and facilitates the transition from high-spin ($t_{2g}^3e_g^2$) Fe(III)N_4 to medium-spin ($t_{2g}^5e_g^1$) Fe(II)N_4 and hence the interaction with the π* antibonding orbitals of oxygen. This leads to a remarkable ORR performance due to optimized desorption of the OH* intermediate on FeN_4, with a half-wave potential of +0.80 in 0.1 M $HClO_4$, in comparison to that with only FeN_4 single-atom moieties. In H_2-O_2 fuel cell tests, a high peak power density of 0.80 W cm^{-2} is obtained. Results from this work highlight the significance of spin engineering in the manipulation and optimization of the ORR activity of single-atom catalysts.

1. Introduction

Development of clean and renewable energy technologies has been attracting extensive interest, as the combustion of conventional fossil fuels has produced significant environmental issues [1–3]. Among these, proton-exchange membrane fuel cells (PEMFCs) have emerged as a viable option [4–6]. Yet, platinum group metals (e.g., Pt/C) are generally required to catalyze the oxygen reduction reaction (ORR) at the cathode, due to complex reaction pathways and sluggish electron-transfer kinetics, resulting in high costs that limit the commercial applications of fuel cells [7,8]. Thus, it is imperative to explore low-cost, high-performance alternatives [9–11], which have been exemplified with metal,nitrogen-codoped carbon composites (MNC, M = Fe, Co, Mn, etc) that are typically derived pyrolytically from select organic and inorganic precursors. Among these, FeNC composites have been found to be a viable option [12,13].

In general, the FeNC composites entail FeN_4 coordination moieties as the active sites. A range of structural engineering has been reported to improve the FeNC activity such that the performance is competitive to commercial benchmarks, especially in acidic media [14–16]. Increasing the number of active sites is one of the effective strategies [15]. For instance, Yang et al. [17] observed an enhanced ORR activity by increasing the iron atom content to 3.5 wt% through a molecularly confined pyrolysis strategy. However, as Fe single atoms are prone to migration and aggregation into particles due to thermodynamic instability in the pyrolysis process [15,16], it is difficult to further increase the content of Fe single atoms and improve the ORR performance. Thus, optimization of the electronic structure of the active sites has emerged as a unique method to improve the intrinsic activity. For example, Hao et al. [18] achieved efficient utilization of active sites and optimization of their electronic structures with carbon vacancy-modified FeNC.

Notably, in pyrolysis at elevated temperatures, the obtained FeNC nanocomposites typically consist of various metal phases ranging from single atoms (SAs) to few-atom clusters (ACs) and to nanoparticles (NPs)

* Corresponding authors.
E-mail addresses: nanwang@jnu.edu.cn (N. Wang), tmh@jnu.edu.cn (H. Meng), shaowei@ucsc.edu (S. Chen).
[1] These authors contributed equally to this work.

https://doi.org/10.1016/j.apcatb.2023.123407
Received 25 July 2023; Received in revised form 27 September 2023; Accepted 18 October 2023
Available online 20 October 2023

[19–23]. Studies have shown that the electronic interactions between Fe SA moieties and adjacent ACs/NPs can drastically enhance the electrocatalytic activity. For example, Huang et al. [24] demonstrated that ACs produced by acid etching of NPs optimized the adsorption energetics of oxygen intermediates of a series of transition-metal single atom catalysts (i.e., Fe, Co, and Ni), leading to improved ORR activity. Zhao et al. [25] showed that the strong interactions between Fe SAs and adjacent Fe NPs led to an appreciable change of the geometric and electronic structure of the Fe-N-C sites, which diminished the energy barrier of the rate-limiting step and enhanced the ORR performance [26]. Such electronic rearrangements at the Fe SA sites can impact the adsorption/desorption energetics and bond lengths of oxygen intermediates, and hence the actual electron-transfer pathways [19]. Moreover, the formation of ACs/NPs adjacent to Fe SA moieties is thermodynamically more favorable than the formation of only Fe SA moieties. Thus, it becomes important to unravel the underlying mechanism of the enhanced ORR performance of the SA active sites by the adjacent ACs/NPs. However, the intimate relationship of how adjacent metal ACs/NPs affect the electronic structure of the Fe SA moieties has remained insufficiently explored.

Theoretically, the kinetic process of ORR involves multiple proton-coupled electron-transfer steps with several key oxygen intermediates (O*, OH*, and OOH*) interacting with the outmost orbitals of the active sites. This suggests that the spin state of the active sites can drastically impact the energetics of adsorption and bond dissociation of the reaction intermediates, and hence the reaction pathways (associative or dissociative) and kinetics, leading to unprecedented manipulation of the ORR activity [27–30]. For example, Yang et al. [29] found that neighboring Mn-N groups changed the Fe active sites from low spin to medium spin through spin state transition and electron modulation, which activated the Fe sites. Wei et al. [27] observed a transition of the Fe(II) atomic sites from low to medium spin by neighboring Pd NPs. He et al. [28] found that the Fe spin state of the FeN_4 moieties could be readily manipulated by metal atoms adjacent to the Fe sites. In these studies, marked enhancement of the ORR activity was observed, which was accounted for by the manipulation of the electronic configuration of the e_g orbitals of the Fe active center. Nevertheless, the underlying mechanism of how adjacent metal species impact the spin state of the Fe SA sites has not been fully understood. This is the primary motivation of this study.

In this study, we prepare a series of nanocomposites where FeN_4 atomic moieties and adjacent Fe few-atom clusters are embedded within a carbon matrix ($Fe_{SA/AC}$@NC) by controlled pyrolysis of an iron-modified zeolitic imidazolate framework (Fe-ZIF-8) precursor. Computational studies based on density functional theory (DFT) calculations show that the octahedral field of the Fe few-atom clusters increases the splitting energy of the parallel tetrahedral field of the FeN_4 moieties, thereby reducing the number of electron fillings in the e_g orbitals and converting Fe(III)N_4/C in the high spin configuration of $t_{2g}^3e_g^2$ to Fe (II) N_4/C in the medium spin ($t_{2g}^5e_g^1$). The resulting $Fe_{SA/AC}$@NC composites indeed exhibit a markedly enhanced electrocatalytic activity towards ORR, with a half-wave potential ($E_{1/2}$) of +0.80 vs. reversible hydrogen electrode (RHE) and long-term stability in acidic media, as compared to traditional FeNC catalysts with only Fe single-atom sites. A membrane electrode assembly (MEA) fabricated with $Fe_{SA/AC}$@NC as the cathode catalyst exhibits a current density of 0.85 A cm^{-2} at 0.7 V (with iR compensation) and a peak power density of 0.80 W cm^{-2} in fuel cell tests. These results highlight the significant impacts of metal few-atom clusters on the spin state of adjacent metal single-atom sites, a unique strategy for the rational design of highly active single atom electrocatalysts.

2. Experimental section

2.1. Chemicals

2-Methylimidazolole, zinc nitrate hexahydrate ($Zn(NO_3)_2{\cdot}6H_2O$), iron nitrate nonahydrate ($Fe(NO_3)_3{\cdot}9H_2O$), methanol and ethanol were purchased from Aladdin. Melamine was purchased from Macklin, and Nafion dispersion (5 wt%) was obtained by diluting a Nafion D2021 dispersion. Isopropyl alcohol and perchloric acid ($HClO_4$) were purchased from Guangzhou Chemical Reagents Factory. Ultra-pure water was provided from a HITECH system (resistivity 18.2 MΩ cm).

2.2. Preparation of graphitic carbon nitride (g-C_3N_4)

The synthetic procedure has been detailed previously [31]. In brief, melamine was heated in a tube furnace at 600 ℃ for 2 h in ambient at a heating rate of 3 ℃ min^{-1}, producing a light yellow powder after grinding.

2.3. Preparation of $Fe_{SA/AC}$@NC nanocomposites

To prepare the Fe-ZIF-8 precursors [32], 2-methylimidazole (240 mmol) was dissolved in 200 mL of methanol under magnetic stirring for 15 min, into which was then added a solution with $Fe(NO_3)_3{\cdot}9H_2O$ (0.5 mmol) and $Zn(NO_3)_2{\cdot}6H_2O$ (28.2 mmol) dissolved in 100 mL of MeOH. The mixture was stirred vigorously for 1 h and then stayed for another 24 h at room temperature. The precipitate was collected by centrifugation, rinsed with methanol several times and then vacuum-dried at 60 ℃ overnight, affording Fe-ZIF-8.

$Fe_{SA/AC}$@NC nanocomposites were synthesized using a high-temperature pyrolysis procedure. In brief, the Fe-ZIF-8 (0.7 g) and g-C_3N_4 (0.14 g) prepared above were mixed by grinding for 30 min and placed in a quartz boat, which was then placed into a tube furnace at 900 ℃ for 1 h with a flow of high-purity nitrogen. The obtained samples were then soaked in a 0.5 M H_2SO_4 solution for 10 h at 70 ℃ to remove metal compounds, before being rinsed with deionized water and ethanol until neutral pH. After vacuum drying at 60 ℃ for 12 h, the samples were heated again in a tube furnace in an ammonia atmosphere at 950 ℃ for 30 min. Fe_{SA}@NC was prepared in the same fashion except that the initial feed of Fe-ZIF-8 was reduced by half (0.35 g). That is, the mass feed ratio of Fe-ZIF-8 to g-C_3N_4 was 5:1 for $Fe_{SA/AC}$@NC and 2.5:1 for Fe_{SA}@NC. A control sample was prepared in the same manner except that the mass feed ratio of Fe-ZIF-8 to g-C_3N_4 was increased to 10:1 and referred to as $Fe_{SA/AC}$@NC(10).

Two additional samples were prepared also in the same manner except that the first pyrolysis was carried out at 800 and 1000 ℃, respectively, and denoted as $Fe_{SA/AC}$@NC-800 and $Fe_{SA/AC}$@NC-1000. For the sample prepared without the addition of Fe-ZIF-8, the product was referred to as NC.

2.4. Characterizations

Scanning electron microscopy (SEM) studies were carried out with a Gemini instrument. Transmission electron microscopy (TEM) images were acquired with a JEM-2100HR microscope operating at 300 kV and a FEI Theims Z aberration-corrected transmission electron microscope (AC-TEM). Energy-dispersive X-ray spectroscopy (EDS) analysis was carried out on a Tecnai G2-F20 equipped with an energy-dispersive X-ray spectroscopy (EDS) detector at an acceleration voltage of 100 kV. Powder X-ray diffraction (XRD) patterns were produced with a Rigaku-D/Max-IIIA diffractometer. Optical absorption was examined with a SHIMADZU ultraviolet-visible (UV–vis) spectrophotometer. Inductively coupled plasma optical emission spectrometry (ICP-OES) measurements were conducted with a PerkinElmer Optima instrument. Brunauer-Emmett-Teller (BET) isotherms were obtained using a Kubo-X1000 instrument. X-ray photoelectron spectroscopy (XPS) experiments were carried out on a Thermo-ESCA-Lab 250 instrument with Al K_α radiation, and C 1s at 284.8 eV was used as a standard to calibrate all XPS data. Raman spectra was obtained using a RENISHAW inVia Qontor Raman spectrometer. X-ray absorption spectra (XAS) studies were carried out at the Taiwan Light Source at room temperature. The obtained XAS data

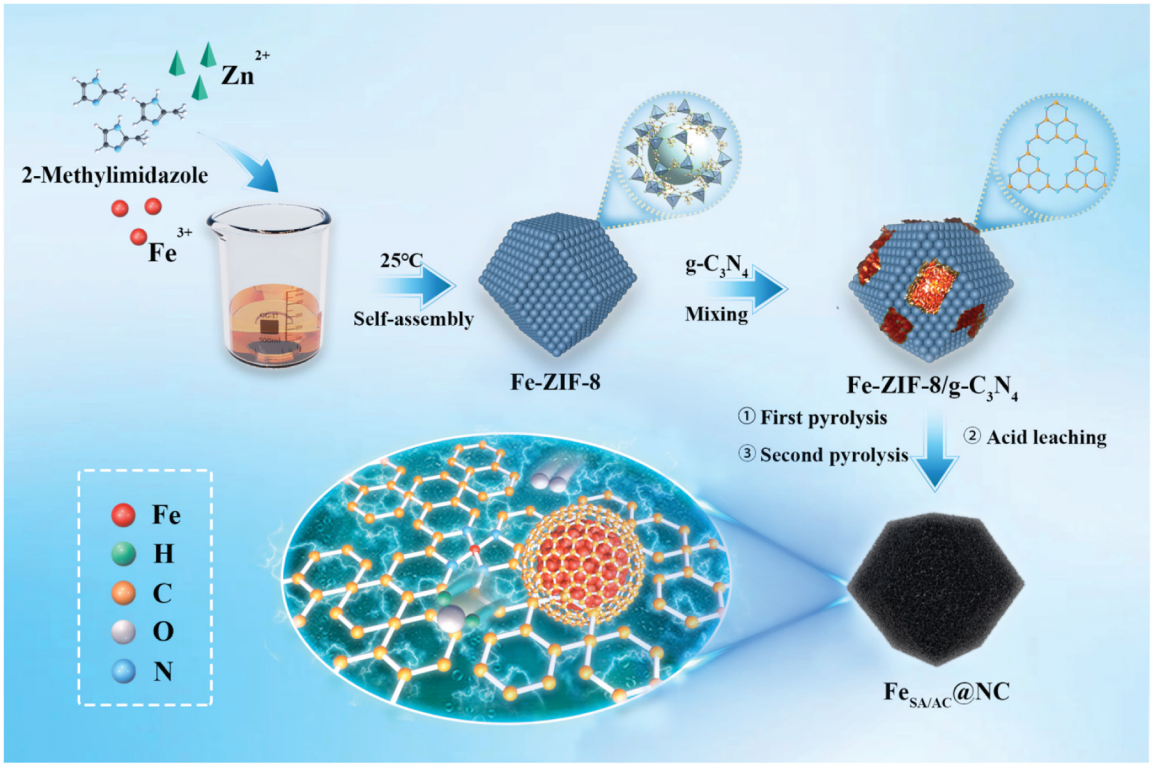

Fig. 1. Schematic illustration of the preparation of $Fe_{SA/AC}$@NC.

were analyzed using the Athena and Artemis software. Electron paramagnetic resonance (EPR) spectra were obtained using a Bruker EMX PLUS Instrument. Magnetism was evaluated with a Quantum Design PPMS-9 instrument.

2.5. Electrochemical measurements

Electrochemical properties were evaluated in a conventional three-electrode cell with a Pine Research Instrument bipotentiostat at room temperature. A glassy carbon electrode (GCE, Pine Research Instrument) with a geometrical area of 0.196 cm^2 was employed as the working electrode. A graphite rod and a Ag/AgCl electrode were employed as the counter electrode and reference electrode, respectively. The Ag/AgCl reference electrode was calibrated against the RHE before each use. To prepare the catalyst ink, 10 mg of the nanocomposites prepared above, 500 μL of isopropanol, and 10 μL of 5 wt% Nafion solution (DuPont) were mixed to form a homogeneous dispersion under sonication for 30 min 5 μL of the ink was dropcast onto the polished surface of GCE, followed by spin-drying naturally at a catalyst loading of 500 μg cm^{-2}. The Pt loading for the commercial Pt/C (40 wt%, Johnson Matthey) was 50 μg cm^{-2}. Linear sweep voltammetry (LSV) curves were recorded at the rotating rates of 400–2500 rpm and a potential sweep rate of 10 mV s^{-1} in 0.1 M $HClO_4$. Chronoamperometric measurements were conducted at +0.7 V vs. RHE.

For the ORR tests, a rotating ring-disk electrode (RRDE, Pine Research Instrument) with a disk area of 0.247 cm^2 was employed as the working electrode, onto which a calculated amount of nanocomposites was deposited, as detailed above. The electron-transfer number (n) and the hydrogen peroxide yield (H_2O_2%) of the ORR were calculated according to previous work [33,34].

2.6. Fuel cell measurements

Catalyst inks were prepared by mixing the nanocomposites obtained above (10 mg), isopropanol, de-ionized water, and 5% Nafion solution at a mass ratio of 1:12:12:11 under sonication for 30 min and stirring for 3 h. The obtained mixture was dropcast onto a gas diffusion layer (GDL, HCP120 Shanghai HESEN) at a loading of 4 mg cm^{-2}. The ratio of Nafion to catalyst (NCR) in the cathode catalyst layer (CCL) was 1:1.82. A commercial Pt anode with 0.5 mg_{Pt} cm^{-2} (Shanghai HESEN) was used as the anode. The MEA was assembled in the order of anode electrode, Nafion 211 membrane (DuPont), and cathode electrode by hot pressing at 135 ℃ for 4 min. The performance test of the fuel cell was carried out at an electronic load (PLZ164WA, KIKUSUI). Both hydrogen and oxygen were humidified at 85 °C to a relative humidity of 100%. Both H_2 on the anode side and O_2 on the cathode side were supplied at a flow rate of 200 sccm under a back pressure of 1 bar (absolute pressure). Cell temperature was stabilized at 80 °C during MEA testing.

2.7. Density functional theory calculations

DFT calculations were performed with the open-source planewave code, Quantum Espresso [35]. In all calculations, the generalized gradient approximation and the projector augments wave pseudopotentials with the exchange and correlation in the Perdew–Burke–Ernzerhof were employed [36–38]. The plane-wave cutoff energy was set at 570 eV. The convergence of forces and energy on each atom during structural relaxation was set at 0.03 eV $Å^{-1}$ in force and 10^{-5} eV in energy, respectively. The Brillouin zone was sampled with 1 × 1 × 1 Monkhorst-Pack k-point grids. The optimized structure size for FeN_4 was 12.29 × 17.04 × 20.00 $Å^3$. The vacuum space along the z[1] direction was more than 15 Å, which was large enough to avoid interplanar interactions. Van der Waals (vdW) interactions were taken into account at the DFT-D_3 level as proposed by Grimme. The obtained results were further corrected by zero-point energy (ZPE). The Gibbs free energy diagrams of ORR were calculated using the method by Nørskov et al. [39]. The free energy were calculated by $\Delta G = \Delta E + \Delta ZPE - T\Delta S + \Delta GU + \Delta G_{pH}$, where ΔE is the total energy, ΔZPE is the variation in zero-point energies and ΔS is the change in entropy before and after the reaction. T is temperature and equals to 298 K. $\Delta GU = eU$, where U is the

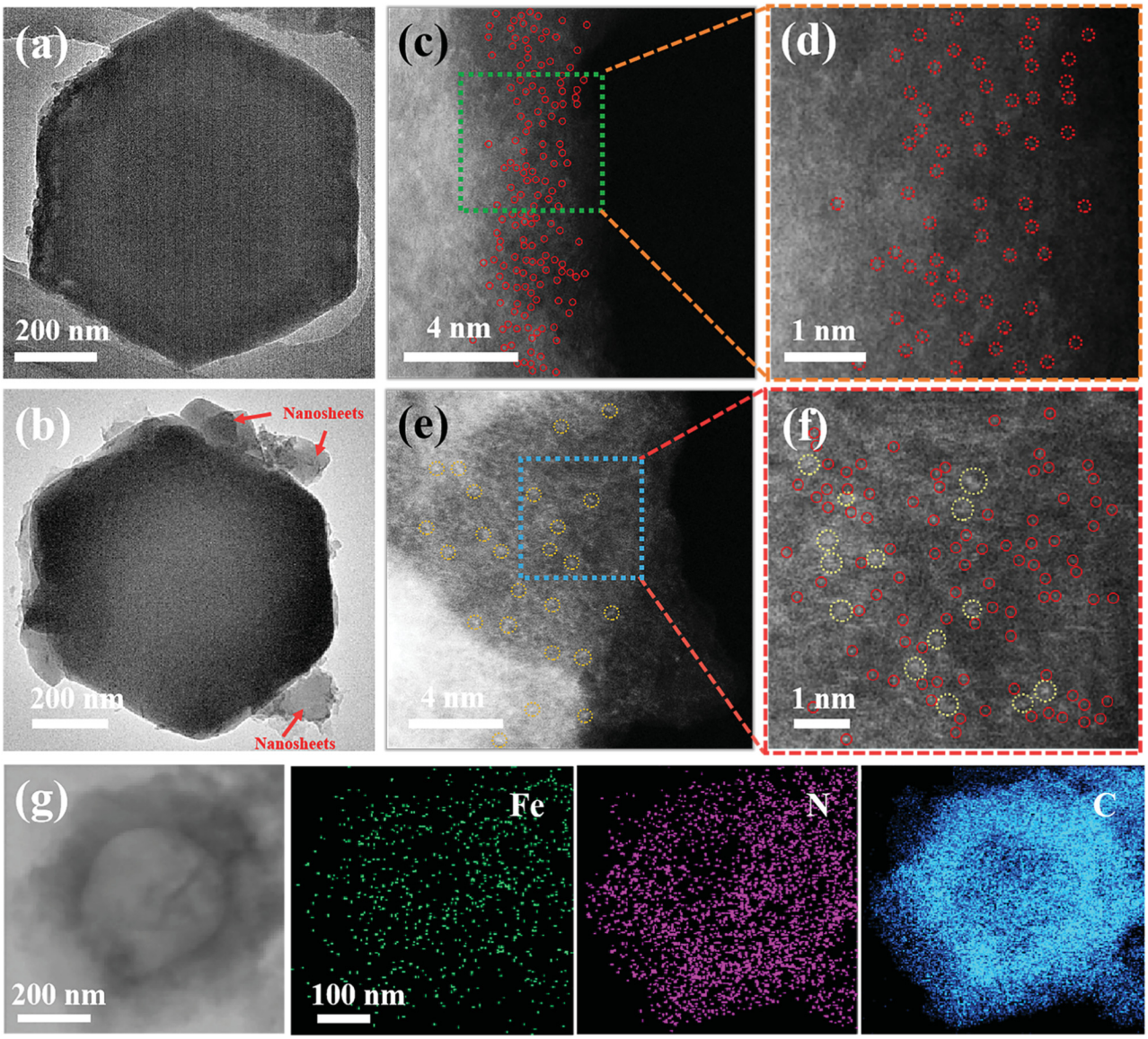

Fig. 2. TEM images of (a) Fe-ZIF-8 and (b) Fe-ZIF-8/g-C_3N_4. AC-TEM images of (c,d) Fe_{SA}@NC and (e,f) $Fe_{SA/AC}$@NC. (g) EDS elemental maps of $Fe_{SA/AC}$@NC (Fe green, N red, and C blue).

electrode potential (vs. standard hydrogen electrode, SHE), e is the electrons transferred in each reaction step. The influence of pH value is ignored in the calculation process.

3. Results and discussion

3.1. Sample preparation

The preparation of $Fe_{SA/AC}$@NC is schematically illustrated in Fig. 1. Fe-modified ZIF-8 (Fe-ZIF-8, Fig. S1a) was first prepared and used as the precursor to prepare $Fe_{SA/AC}$@NC nanocomposites. This was aided by the addition of graphitic carbon nitride (g-C_3N_4, Fig. S1b) that acted as a nitrogen source to generate ammonia during pyrolysis that etched the sample surface, enriched the surface nitrogen content, produced defects, and hindered the agglomeration of Fe during pyrolysis. The procedure consisted of a first pyrolysis at 900 °C, followed by acid leaching and then a second pyrolysis at 950 °C. A comparative sample containing only Fe SA sites was prepared in the same manner except that the initial feed of Fe-ZIF-8 was reduced by half, which was denoted as Fe_{SA}@NC.

3.2. Structural characterization

The Fe-ZIF-8 sample retained the rhombic dodecahedron shape of the pristine ZIF-8 crystals, but the size of the particles (ca. 500 nm) was markedly larger than that of the undoped counterpart (350 nm) (Fig. 2a and S1-S2) [23,40]. Also, mechanical mixing with g-C_3N_4 did not impact the morphology of Fe-ZIF-8 (Fig. 2b, S1c and S3-S4). After Fe-ZIF-8/g-C_3N_4 was pyrolyzed at high temperatures, the resulting $Fe_{SA/AC}$@NC nanocomposites retained the skeleton structure, but the size was significantly reduced to only ca. 350 nm, and the faces of the dodecahedron contracted inward, forming a curved polyhedron morphology with curved eaves (Fig. S5), most likely due to the anisotropic thermal shrinkage of the Fe-ZIF-8 precursor, where the edges and vertices of the dodecahedron were subject to less stress than the faces during pyrolysis [41–43]. In XRD measurements, only the carbon diffraction peaks were resolved with the $Fe_{SA/AC}$@NC and Fe_{SA}@NC samples (Fig. S6), suggesting the lack of large Fe nanoparticles within the carbon matrix.

Consistent structural insights were obtained from AC-TEM measurements. One can see from Fig. 2c-d that Fe_{SA}@NC consisted of a large

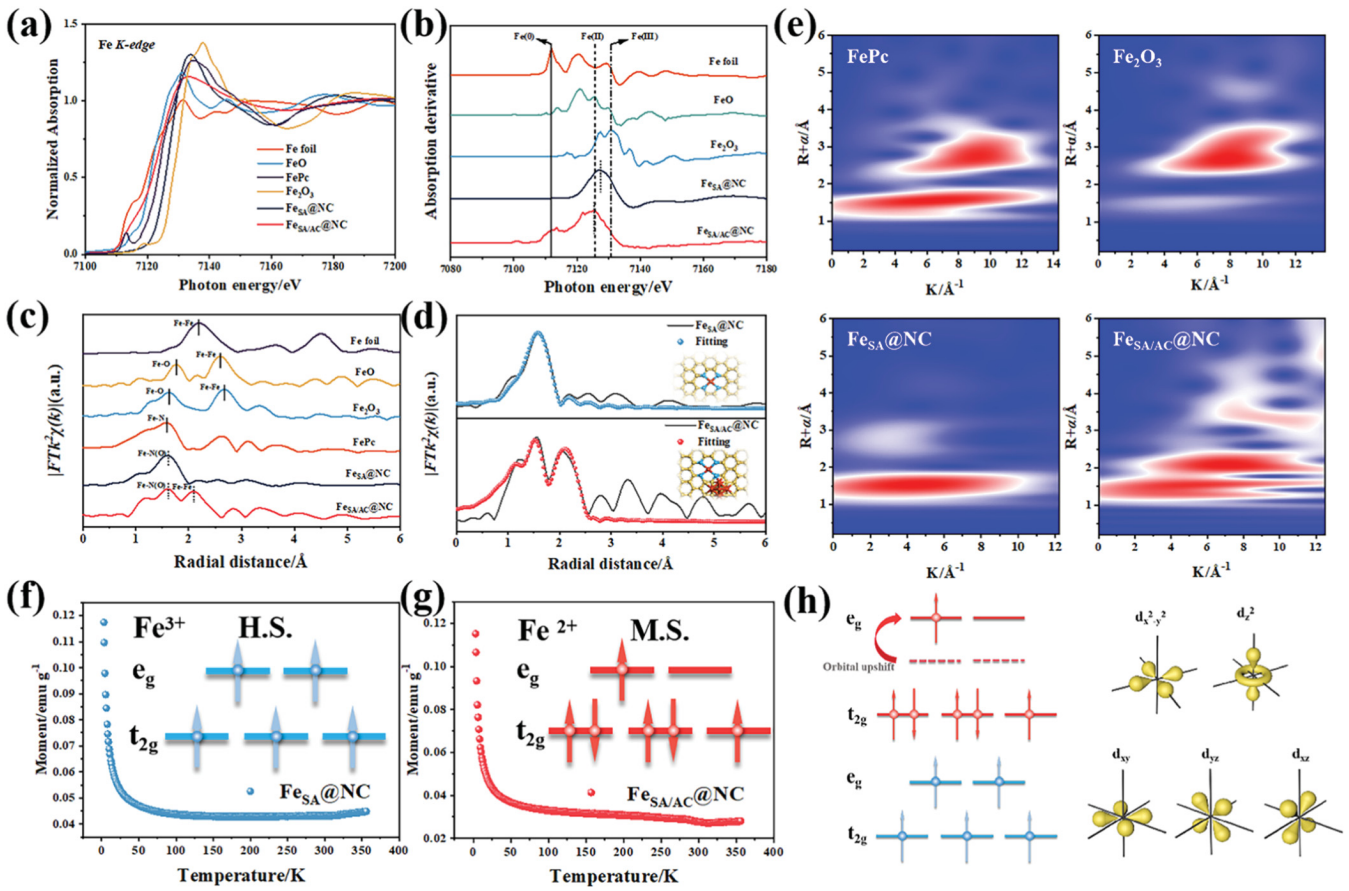

Fig. 3. (a) Normalized Fe K-edge XANES spectra, (b) first-order derivatives of the XANES spectra, and (c) Fe K-edge Fourier-transform k^2-weighted EXAFS spectra of Fe foil, FePc, FeO, Fe_2O_3, Fe_{SA}@NC and $Fe_{SA/AC}$@NC. (d) Fitting results of the magnitude of the Fourier transform of the k^2-weighted EXAFS for Fe_{SA}@NC and $Fe_{SA/AC}$@NC. Insets show the schematics of the respective structure. (e) WT-EXAFS of Fe_{SA}@NC, $Fe_{SA/AC}$@NC, FePc, and Fe_2O_3. Magnetization intensity of (f) Fe_{SA}@NC and (g) $Fe_{SA/AC}$@NC (H.S. represents high-spin, M.S. represents medium-spin). (h) Schematic diagram of structural transformation of high spin and medium spin Fe states.

number of light-contrast dots (highlighted by red circles) without any nanoparticulates, most likely arising from iron atomic species that possessed a higher electron density than the carbon matrix. By contrast, for $Fe_{SA/AC}$@NC that was prepared at a higher feed of Fe-ZIF-8 in sample synthesis (Fig. 2e-f), both Fe atomic species (highlighted by red dashed circles) and few-atom clusters (highlighted by yellow dashed circles, ca. 0.8 nm in diameter) can be resolved [26,44]. In EDS-based elemental mapping analysis (Fig. 2g), the elements of Fe, C and N can be seen to be uniformly distributed across the sample, suggesting that the iron species were embedded within a N-doped carbon scaffold most likely in the forms of single atoms and/or few-atom clusters.

In Raman spectroscopic measurements, the samples all exhibited two major peaks at ca. 1350 and 1595 cm^{-1} (Table S1 and Fig. S7), due to the D and G bands of graphitic carbon, confirming the successful transformation of the Fe-ZIF-8 precursors into carbon materials. Additionally, the intensity ratio of the D and G bands (I_D/I_G) was found to be close for Fe_{SA}@NC and $Fe_{SA/AC}$@NC at 1.04 and 1.01, respectively, indicating a similar degree of graphitization of the two samples. In nitrogen adsorption/desorption measurements (Table S2 and Fig. S8-S9), $Fe_{SA/AC}$@NC can be found to exhibit a type IV isotherm, indicating the formation of abundant micropores and mesopores, with a high specific surface area of 1168.23 $m^2\ g^{-1}$, and Fe_{SA}@NC possessed an even larger specific area of 2352.19 $m^2\ g^{-1}$, likely due to formation of ACs in the former that occupied the defect sites [45–47]. In comparison, the metal-free N-doped carbon (NC) prepared from C_3N_4 without the addition of Fe-ZIF-8 showed a specific surface area of only 857.22 $m^2\ g^{-1}$ (Table S2) [48–50]. This signifies the unique porogenic impacts of Fe species (from Fe-ZIF-8) in enhancing the porosity of the nanocomposites.

The elemental composition and valency of the samples were then investigated by XPS measurements. From the survey spectra of Fe_{SA}@NC and $Fe_{SA/AC}$@NC (Fig. S10), the Fe 2p, N 1s, C 1s and O 1s electrons can be clearly identified at 710.1, 400.1, 284.4, and 531.9 eV, respectively. The corresponding elemental contents are listed in Table S3, where both samples can be seen to consist of about 90 at% C, with slightly more Fe in $Fe_{SA/AC}$@NC (0.2 at%) than in Fe_{SA}@NC (<0.2%), consistent with results from ICP-OES measurements where the Fe content was 2.6 wt% for the former and 2.3 wt% for the latter. The C 1s profiles are also very consistent (Fig. S11a). From the high-resolution N 1s spectra in Fig. S11b, five N species can be deconvoluted with $Fe_{SA/AC}$@NC, pyridine nitrogen (398.10 eV), Fe-N (398.70 eV), pyrrole nitrogen (399.55 eV), graphite nitrogen (401.50 eV) and nitrogen oxide (402.50 eV) (Table S4). A similar structure can be found with Fe_{SA}@NC, suggesting that Fe was anchored into the carbon skeleton forming FeN_x moieties. Nevertheless, one can see that $Fe_{SA/AC}$@NC possessed a somewhat lower binding energy of the Fe-N species (398.70 eV) than Fe_{SA}@NC (398.90 eV), suggesting enrichment of the Fe electron density likely due to the adjacent Fe clusters. From the Fe 2p spectra in Fig. S12, the Fe^{2+} and Fe^{3+} $2p_{3/2}$ binding energy can be found at 710.51 and 713.44 eV for $Fe_{SA/AC}$@NC, in comparison to 711.14 and 714.75 eV for Fe_{SA}@NC. Moreover, the atomic ratio of Fe^{2+}/Fe^{3+} can be found to increase from 70.7% in the latter to 85.9% in the former (Table S5). Taken together, these results suggest a reduced valence (and spin state) of the Fe atomic centers by the adjacent few-atom Fe clusters.

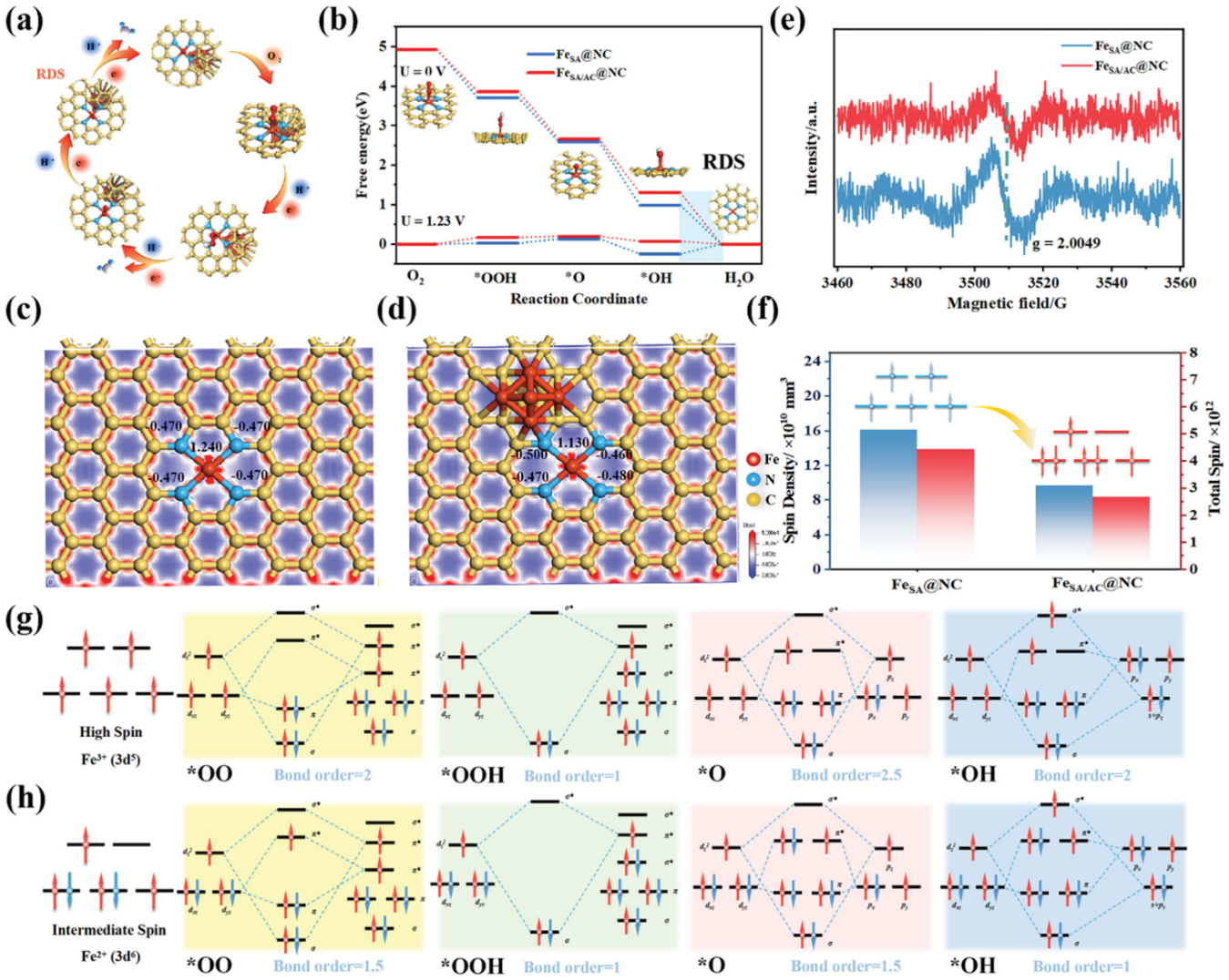

Fig. 4. Computational analysis of $Fe_{SA/AC}$@NC. (a) Schematic illustration of ORR mechanism on $Fe_{SA/AC}$@NC. (b) Free energy diagram of ORR on Fe_{SA}@NC and $Fe_{SA/AC}$@NC at 1.23 and 0 V vs. RHE. Calculated charge density differences for (c) Fe_{SA}@NC and (d) $Fe_{SA/AC}$@NC. (e) EPR spectra of Fe_{SA}@NC and $Fe_{SA/AC}$@NC. (f) Total spin and spin density for Fe_{SA}@NC and $Fe_{SA/AC}$@NC derived from the EPR results. The formation of chemical bonds with oxygen-related intermediates in (g) high-spin Fe^{3+} and (h) intermediate-spin Fe^{2+} species at the edge sites. The bond order is defined as $\frac{(n_{bonding}-n_{anti-bonding})}{2}$, where $n_{bonding}$ and $n_{anti\text{-}bonding}$ denote the number of electrons in the bonding or anti-bonding orbitals. The bigger the bonder order, the stronger the bond strength.

The atomic configuration of the Fe sites of the nanocomposites was further investigated by XAS measurements. From the X-ray absorption near-edge spectra (XANES) in Fig. 3a, it can be seen that the Fe *K*-edge of Fe_{SA}@NC lies between those of FeO and Fe_2O_3, indicating that the oxidation state of Fe is between + 2 and + 3. For comparison, the absorption edge of $Fe_{SA/AC}$@NC was at a somewhat lower energy and closer to that of FeO, in good agreement with results from the above XPS measurements that showed a higher Fe^{2+}/Fe^{3+} ratio. The evolution of the oxidation state can be seen more clearly based on the first order derivative of the XANES spectrum (Fig. 3b). In k^2-weighted extended X-ray absorption fine structure (EXAFS) measurements (Fig. 3c), Fe_{SA}@NC shows only a dominant peak in the R space at ca. 1.5 Å, most likely arising from the Fe-N/O scattering path, and the absence of Fe-Fe paths confirms the formation of single Fe atomic sites in the sample. By contrast, in addition to the Fe-N/O peak, $Fe_{SA/AC}$@NC also exhibited a peak close to 2.3 Å that can be ascribed to the Fe-Fe path, in good agreement with the formation of Fe clusters in the samples (Fig. 3d and Table S6), as manifested in the above TEM measurements (Fig. 2). Fitting of the EXAFS data shows that the coordination number (CN) of Fe-N/O was about 4.11 for Fe_{SA}@NC, and 3.72 for $Fe_{SA/AC}$@NC, both close to 4 (and the Fe-Fe CN of the latter was 1.97). In wavelet transform EXAFS analysis (Fig. 3e and S13), Fe_{SA}@NC exhibited only one intensity maximum at around 4.0 $Å^{-1}$, consistent with the structure analogous to that of iron porphyrin (FePc), suggesting the formation of Fe single atom moieties in the form of FeN_4; whereas $Fe_{SA/AC}$@NC displayed a second intensity maximum at ca. 7.3 $Å^{-1}$, due to Fe-Fe scattering. The negative shift in *K* values (ca. 8 $Å^{-1}$) from the Fe-Fe bonds in iron foils likely arose from the different coordination environments of the iron species in the clusters [19,30,51]. Taken together, these results confirmed the formation of both Fe SAs and ACs in $Fe_{SA/AC}$@NC whereas only SAs in Fe_{SA}@NC.

The electronic properties of the samples were further examined by UV–vis diffuse reflectance spectroscopy (DRS) measurements [52–54]. From Fig. S14, the band gap was estimated to be about 1.8 eV for Fe_{SA}@NC and somewhat higher at 1.91 eV for $Fe_{SA/AC}$@NC, suggesting an increase of the splitting of the planar quadrilateral field of the FeN_4 moieties [54,55]. The increase of the e_g orbital energy suggests reduced filling of electrons in the orbital and hence a variation of the sample spin state, which was further confirmed in zero-field cooling (ZFC) temperature-dependent magnetization measurements. At low

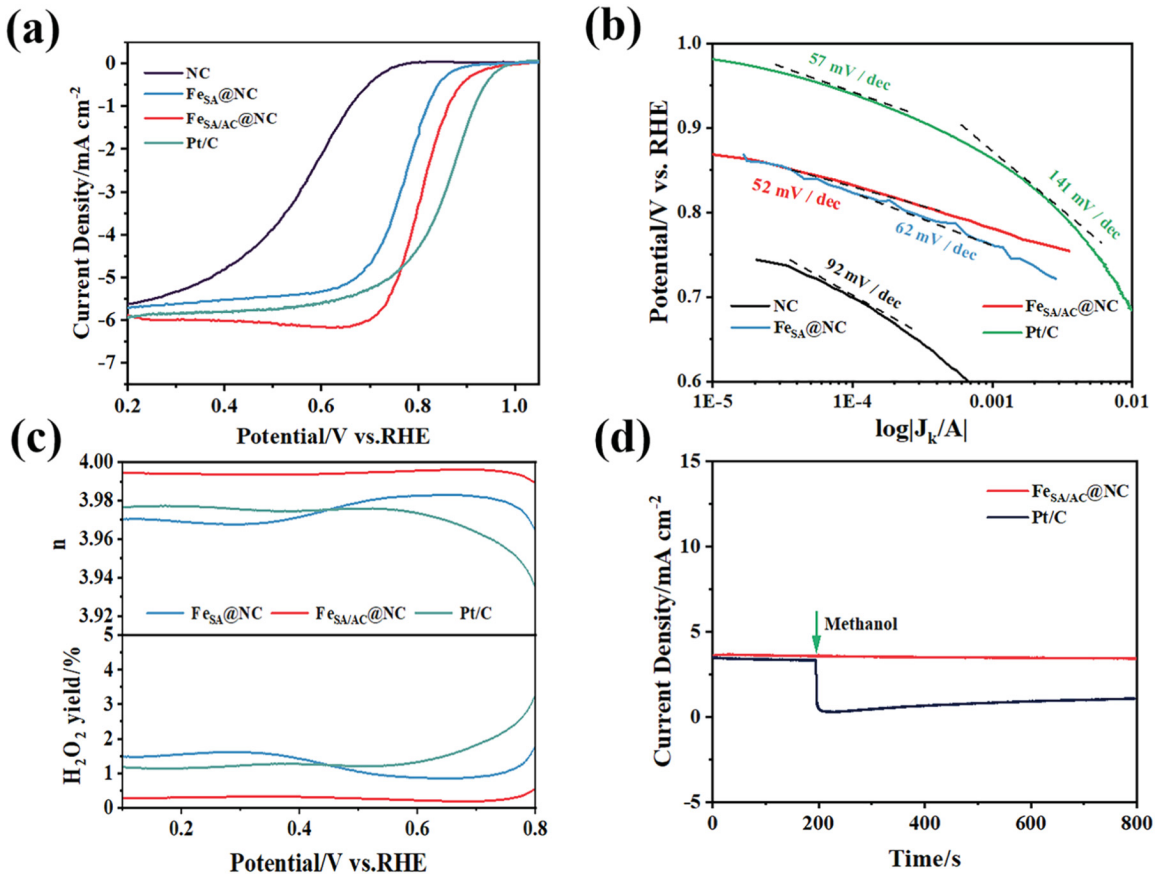

Fig. 5. Electrochemical performance of the catalyst. (a) LSV polarization curves in O_2-saturated 0.1 M $HClO_4$ solution at 1600 rpm. (b) Tafel curves (kinetic region: 0.6–1.1 V vs. RHE). (c) H_2O_2 yield and electron transfer number from RRDE measurements. (d) Methanol tolerance tests of $Fe_{SA/AC}$@NC and Pt/C 40 wt%.

temperatures (Fig. S15), Fe_{SA}@NC shows a stronger Curie tail than $Fe_{SA/AC}$@NC. This clearly indicates a decrease of the number of free electrons in the latter. In fact, the effective magnetic moment (μ_{eff}) was estimated to be 5.92 μ_B for Fe_{SA}@NC, whereas only 3.25 μ_B for $Fe_{SA/AC}$@NC. This suggests that the crystal field of the planar quadrilateral FeN_4 becomes stronger with the formation of Fe clusters, which increases the splitting and the e_g orbital energy, makes it difficult for electrons to fill the high-energy orbitals, and leads to a decrease of the spin state. According to the equation $\mu_{eff} = \sqrt{n(n+2)}$ [27,29], the number of unpaired d electron (n) was estimated to be about 5.0 and 2.4, respectively. In combination with the valence analysis in XANES measurements (Fig. 3a-b), it can be concluded that the FeN_4 moieties in Fe_{SA}@NC are in a high-spin state, with a high degree of e_g filling ($d_z^2 1$ $d_{xy}^2 1$); whereas only in medium spin in $Fe_{SA/AC}$@NC with the e_g configuration of $d_{xy}2$ $d_{yz}2$ $d_{xz}1$ $d_z^2 1$. Note that the single dz^2 electrons in the medium-spin state can easily interact with the π* antibonding orbital of oxygen, resulting in a high ORR activity (vide infra). As transition metals mostly possess an octahedral field [56–58], this suggests that the introduction of octahedral atomic clusters in the planar tetragonal field can increase the splitting of the planar tetragonal field, reduce the electron leap to the e_g orbitals and thus change the spin state of the planar tetragonal field, leading to an improved performance in ORR.

3.3. Computational study

To further understand the influence of Fe clusters on the spin state of FeN_4, DFT calculations were carried out to construct the free energy diagrams (Fig. 4a). From Fig. 4b, it can be seen that the ORR paths are downhill for all samples at 0 V, suggestive of the exothermic and spontaneous nature; whereas at 1.23 V, the fourth step can be seen to possess the largest free energy barrier (Table S7), suggesting that the desorption of OH* ($OH^* + H^+ + e^- \rightarrow H_2O$) from the active site is the rate determining step (RDS).

Although the RDS is the same for all samples at 0 V (Fig. 4b and Table S7), the free energy change for $Fe_{SA/AC}$@NC (−1.30 eV) is lower than that for Fe_{SA}@NC (−0.98 eV), suggesting that $Fe_{SA/AC}$@NC is thermodynamically more favorable as the atomic cluster likely acts as an activity booster. Indeed, electron redistribution is observed in charge density analysis (Fig. 4c-d), where electron transfer occurs from the Fe SA centers in Fe_{SA}@NC to the adjacent carbon substrate, making the Fe centers electron-deficient. Yet in $Fe_{SA/A}$C@NC (Fig. 4d), the Fe SA centers are actually richer in electron density, due to electron donation from the Fe clusters to the FeN_4 sites, in good agreement with results from the above XANES measurements. Note that electron-enriched Fe sites facilitate electron transfer to the oxygen p* orbitals and the formation of peroxide rather than superoxide intermediates, which is preferred for the cleavage of the O-O bond and four-electron reduction pathway of ORR [59–61].

Consistent results were obtained in EPR measurements. Fe_{SA}@NC and $Fe_{SA/AC}$@NC both exhibited obvious signals near the magnetic field intensity of 3500 G (Fig. 4e), indicating the existence of unpaired electrons in both materials. Yet, the peak-to-peak intensity was higher in the former than in the latter, suggesting more unpaired electrons in Fe_{SA}@NC than in $Fe_{SA/AC}$@NC (Fig. 4f). Notably, an even lower signal was observed with $Fe_{SA/AC}$@NC(10) that was prepared at a higher Fe-ZIF-8 to g-C_3N_4 feed ratio, suggesting that the Fe atomic sites were likely in the low-spin state (Fig. S16). This is in accord with the afore-mentioned variation of the Fe spin states due to electron transfer from the adjacent Fe clusters — $Fe_{SA/AC}$@NC(10) even contained a substantial amount of metallic Fe most likely in the form of larger nanoparticles (Fig. S12). The

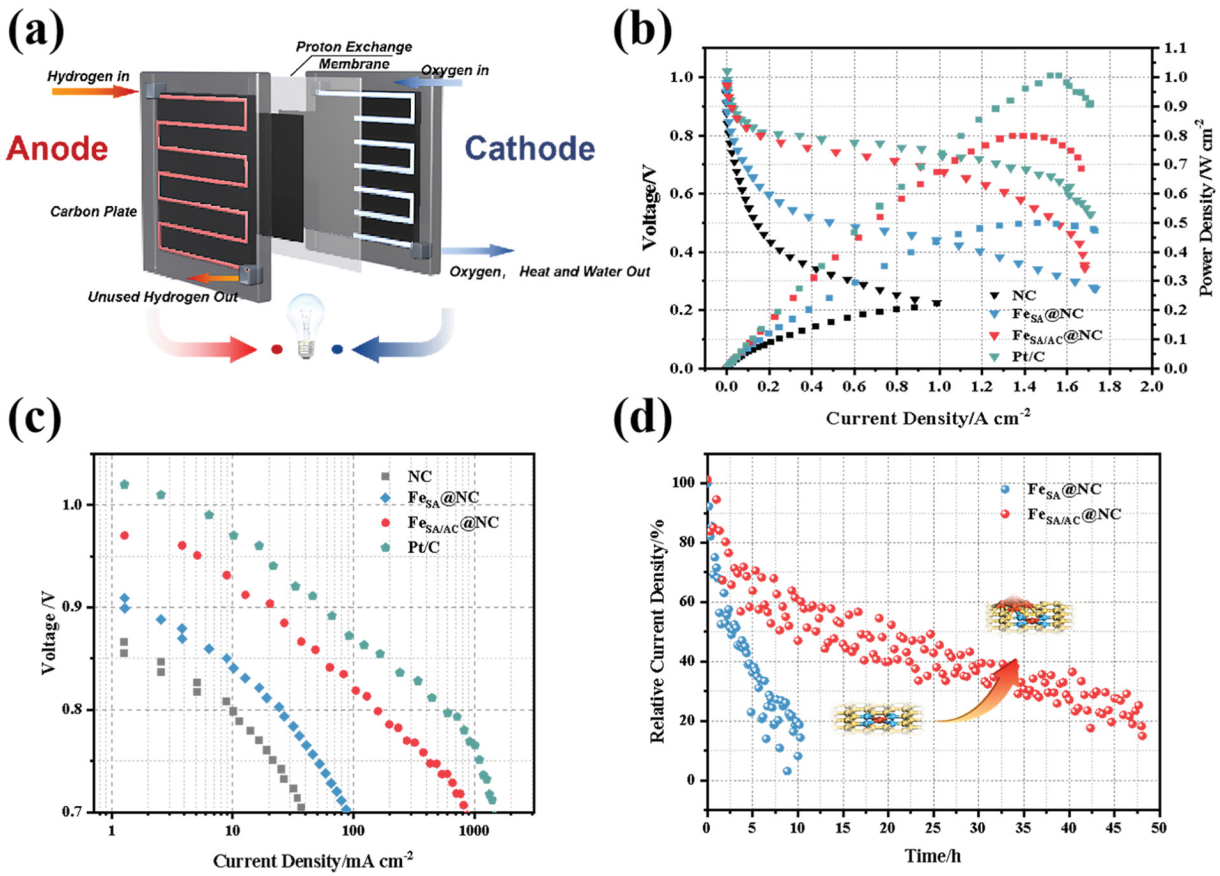

Fig. 6. (a) Proton exchange membrane fuel cell model. (b-c) The polarization curves and power density plots of NC, Fe_{SA}@NC, $Fe_{SA/AC}$@NC and Pt/C. (d) Stability test of $Fe_{SA/AC}$@NC at a constant voltage of 0.6 V under 1 bar_{abs} H_2-O_2. The measurements are performed at T_{cell} = 70 °C, 100% RH, $P_{cathode}$ = P_{anode} = 1 bar_{abs}, with the H_2 and O_2 flow rate at 120 and 150 mL min^{-1}, respectively.

relationship between the Fe d orbitals of Fe_{SA}@NC and $Fe_{SA/AC}$@NC and the adsorption intermediate orbitals is shown in Fig. 4g-h. For the high-spin Fe(III)N_4 sites of Fe_{SA}@NC, the e_g and t_{2g} orbitals were semi-filled forming a $t_{2g}^3e_g^2$ configuration, and upon the adsorption of oxygen intermediates, the bonds are stronger because the bond order with high-spin Fe(III)N_4 is greater than that with medium-spin Fe(II)N_4. Note that stronger adsorption of intermediate products may be unfavorable for product desorption and hence compromise the ORR activity (vide infra), as the RDS is step 4, desorption of OH species (Fig. 4b). This is indeed manifested in electrochemical measurements (vide infra).

Since the interaction between Fe^{3+} and oxygen intermediate is proportional to the bond order, the adsorption of $*O_2$ on Fe(III)N_4 is as strong as that of *OH. However, medium-spin Fe(II)N_4 shows stronger adsorption of $*O_2$ than of *OH, rendering it energetically more feasible to capture the reactants and release the products from a thermodynamic point of view. In addition, the stability of the active sites was studied within the context of bond length stretching and shrinking. As shown in Table S8, the average length of the Fe-N bond of FeN_4 in Fe_{SA}@NC is 1.970 Å, significantly longer than that in $Fe_{SA/AC}$@NC (1.879 Å), consistent with the fitting results of the EXAFS data (Table S5). This indicates that the Fe-N bond is more stable in $Fe_{SA/AC}$@NC, as demetalization typically starts from the stretching and breaking of the Fe-N bond [19,24,62].

3.4. ORR activity and PEMFC performance

The electrocatalytic performance of the series of composites was then studied and compared. As shown in Fig. 5a, the metal-free NC exhibited a minimal activity with nonzero currents starting to appear at ca. + 0.7 V in 0.1 M $HClO_4$; and the performance was markedly enhanced with Fe_{SA}@NC, indicating dominant contributions from the Fe single atoms. The $Fe_{SA/AC}$@NC sample exhibited an even better performance, featuring an onset potential (E_{onset}) of +0.93 V and a half-wave potential ($E_{1/2}$) of +0.80 V, in comparison to Fe_{SA}@NC ($E_{1/2}$ = +0.77 V). The corresponding turnover frequency (TOF) was estimated to be 0.47 e^- $site^{-1}$ s^{-1} for the former and 0.36 e^- $site^{-1}$ s^{-1} for the latter (Fig. S17), confirming the positive impact of adjacent Fe clusters on the ORR activity of Fe SA sites. Note that the performance of $Fe_{SA/AC}$@NC is only somewhat lower as compared to that of commercial Pt/C 40 wt% ($E_{1/2}$ = +0.86 V). In fact, $Fe_{SA/AC}$@NC represented the optimal sample within the context of C_3N_4 initial feed (e.g., $Fe_{SA/AC}$@NC(10)) and pyrolysis temperature (e.g., $Fe_{SA/AC}$@NC-800 and $Fe_{SA/AC}$@NC-1000), consistent with the variation of their spin properties (Figs. S16 and S18). The corresponding Tafel plots are shown in Fig. 5b, where $Fe_{SA/AC}$@NC exhibited a Tafel slope of 52 mV dec^{-1}, somewhat lower than those of FeSA@NC (62 mV dec^{-1}) and even Pt/C (57 mV dec^{-1}), indicating slightly faster electron-transfer kinetics.

In RRDE tests, the electron transfer number of ORR was estimated to be 3.99 on $Fe_{SA/AC}$@NC, indicating that ORR followed the 4e^- pathway, and the corresponding hydrogen peroxide yield was minimal at less than 0.5% within the potential range of +0.1 to +0.8 V, much lower than that (0.6–1%) for others in the sample series (Fig. 5c). To verify that the reaction step of the catalyst is dominated by the 4e^- process, polarization curves were collected at different rotation rates (Fig. S19). The calculations based on the Koutecky-Levich (K-L) equation indeed confirm that ORR on $Fe_{SA/AC}$@NC primarily followed the 4e- pathway. Notably, no significant change was observed in the methanol tolerance test with $Fe_{SA/AC}$@NC, whereas a sharp diminishment of the current density was

observed under the same conditions with Pt/C, indicating remarkable methanol tolerance by $Fe_{SA/AC}$@NC (Fig. 4d). The $Fe_{SA/AC}$@NC sample also exhibited remarkable stability. In chronoamperometric tests at +0.70 V in 0.1 M $HClO_4$ (Fig. S20), 86% of the initial current density were retained for $Fe_{SA/AC}$@NC after continuous operation for 50,000 s, in comparison to 77% for Fe_{SA}@NC and only 61% for Pt/C.

The prepared FeNC composites were then used as the cathode catalyst and commercial Pt/C as anode catalyst to construct a membrane electrode assembly (MEA) for a H_2-O_2 fuel cell (Fig. 6a; details in the Supporting Information). From Fig. 6b it can be seen that the fuel cell reached a peak power density of 0.8 W cm^{-2} for $Fe_{SA/AC}$@NC, which was markedly higher than those for Fe_{SA}@NC (0.5 W cm^{-2}) and metal-free NC (0.25 W cm^{-2}) but remained subpar as compared to that of commercial Pt/C (1.01 W cm^{-2}). Such performances are markedly better than a number of relevant catalysts reported previously (Table S9). As can be seen from Fig. 6c, the $Fe_{SA/AC}$@NC cell exhibits a current density up to 0.85 A cm^{-2} at 0.7 V, much higher than others, Fe_{SA}@NC (0. 09 A cm^{-2}) and NC (0.04 A cm^{-2}) but lower than that of Pt/C (1.05 A cm^{-2}). In fact, $Fe_{SA/AC}$@NC represent the optimal composition within the preset experimental context (Fig. S21).

The stability of the nanocomposites in fuel cell was then evaluated by holding the voltage at 0.7 V for up to 48 h. From Fig. 6d, it can be seen that $Fe_{SA/AC}$@NC clearly outperformed Fe_{SA}@NC within this long period of operation, although the current density exhibited an apparent decay. Further studies are desired to unravel the deactivation mechanism and to enhance the structural integrity of the FeNC catalysts during long-term operation.

4. Conclusion

In summary, highly stable and active FeNC nanocomposites were prepared as ORR catalysts for PEMFC, where Fe few-atom clusters were found to drastically impact the spin state of the adjacent Fe single atom sites and enhance the ORR activity and fuel cell performance. Specifically, the cluster-free Fe_{SA}@NC was found to consist primarily of a Fe (III)-$e_g^2t_{2g}^3$ configuration with a relatively low splitting energy. Yet, with the formation of adjacent Fe few-atom clusters, the octahedral field of Fe ACs markedly enhanced the crystal field of the Fe SA sites in $Fe_{SA/AC}$@NC, resulting in the electrons rearrangement and a Fe(II)-$e_g^1t_{2g}^5$ configuration. This resulted in optimization of the adsorption/desorption of key oxygen intermediates and RDS energetics, leading to a remarkable ORR performance and good stability in acidic media and a maximum power density of 0.8 W cm^{-2} as a fuel cell cathode and excellent stability in PEMFC. Results from this work, through a deliberate integration of theory and experiment, highlight the significance of structural engineering in the manipulation of the spin state of Fe atomic centers in FeNC composites and hence optimization of the electrocatalytic performance. Such unique mechanistic insights can be exploited for the rational design of high-performance catalysts and advance electrochemical energy technologies.

CRediT authorship contribution statement

Chengjie Chen: Data curation, Formal analysis, Writing – original draft. **Yinlong Wu**: Data curation, Formal analysis, Writing – original draft. **Xiulan Li**: Data curation, Formal analysis. **Yanting Ye**: Data curation, Formal analysis. **Zilong Li**: Data curation. **Yifan Zhou**: Formal analysis. **Jian Chen**: Formal analysis. **Muzi Yang**: Formal analysis. **Fangyan Xie**: Formal analysis. **Yanshuo Jin**: Formal analysis. **Colton Jones**: Formal analysis. **Nan Wang**: Conceptualization, Methodology, Formal analysis, Funding acquisition, Writing – original draft. **Hui Meng**: Conceptualization, Methodology, Formal analysis, Funding acquisition, Writing – original draft. **Shaowei Chen**: Conceptualization, Methodology, Formal analysis, Resources, Writing – review & editing.

Declaration of Competing Interest

The authors declare that they have no known competing financial interests or personal relationships that could have appeared to influence the work reported in this paper.

Data availability

Data will be made available on request.

Acknowledgments

This work was supported by the National Natural Science Foundation of China (22075102, 22005120, 21576301, 51973244, 22209056); the Fundamental Research Funds for the Central Universities (21620329, 21621007); the Postdoctoral Research Foundation of China (2020M673071); the Special Funds for the Cultivation of Guangdong College Students' Scientific and Technological Innovation (pdjh2022b0065); the Guangdong Basic and Applied Basic Research Foundation (2022A1515010523, 2023A1515010270); the Science and Technology Planning Project of Guangzhou (201605030008, 202201010360) and the National Innovation and Entrepreneurship Training Program for Undergraduate (202110559044). S.W.C. thanks the National Science Foundation for partial support of the work (CHE-1900235, CHE-2003685).

Appendix A. Supporting information

Supplementary data associated with this article can be found in the online version at doi:10.1016/j.apcatb.2023.123407.

References

[1] C. Niether, S. Faure, A. Bordet, J. Deseure, M. Chatenet, J. Carrey, B. Chaudret, A. Rouet, Improved water electrolysis using magnetic heating of FeC–Ni core–shell nanoparticles, Nat. Energy 3 (2018) 476–483.
[2] Y. Wang, H. Su, Y. He, L. Li, S. Zhu, H. Shen, P. Xie, X. Fu, G. Zhou, C. Feng, D. Zhao, F. Xiao, X. Zhu, Y. Zeng, M. Shao, S. Chen, G. Wu, J. Zeng, C. Wang, Advanced electrocatalysts with single-metal-atom active sites, Chem. Rev. 120 (2020) 12217–12314.
[3] Y. Chen, Z. Li, Y. Zhu, D. Sun, X. Liu, L. Xu, Y. Tang, Atomic Fe dispersed on N-doped carbon hollow nanospheres for high-efficiency electrocatalytic oxygen reduction, Adv. Mater. 31 (2019), e1806312.
[4] A. Kulkarni, S. Siahrostami, A. Patel, J.K. Norskov, Understanding catalytic activity trends in the oxygen reduction reaction, Chem. Rev. 118 (2018) 2302–2312.
[5] M. Shao, Q. Chang, J.P. Dodelet, R. Chenitz, Recent advances in electrocatalysts for oxygen reduction reaction, Chem. Rev. 116 (2016) 3594–3657.
[6] Y. He, S. Liu, C. Priest, Q. Shi, G. Wu, Atomically dispersed metal–nitrogen–carbon catalysts for fuel cells: advances in catalyst design, electrode performance, and durability improvement, Chem. Soc. Rev. 49 (2020) 3484–3524.
[7] H.A. Gasteiger, S.S. Kocha, B. Sompalli, F.T. Wagner, Activity benchmarks and requirements for Pt, Pt-alloy, and non-Pt oxygen reduction catalysts for PEMFCs, Appl. Catal. B: Environ 56 (2005) 9–35.
[8] M.K. Debe, Electrocatalyst approaches and challenges for automotive fuel cells, Nature 486 (2012) 43–51.
[9] Y. Deng, B. Chi, X. Tian, Z. Cui, E. Liu, Q. Jia, W. Fan, G. Wang, D. Dang, M. Li, K. Zang, J. Luo, Y. Hu, S. Liao, X. Sun, S. Mukerjee, g-C3N4 promoted MOF derived hollow carbon nanopolyhedra doped with high density/fraction of single Fe atoms as an ultra-high performance non-precious catalyst towards acidic ORR and PEM fuel cells, J. Mater. Chem. A 7 (2019) 5020–5030.
[10] J.W. Su, R.X. Ge, Y. Dong, F. Hao, L. Chen, Recent progress in single-atom electrocatalysts: concept, synthesis, and applications in clean energy conversion, J. Mater. Chem. A 6 (2018) 14025–14042.
[11] X.Q. Wang, Z.J. Li, Y.T. Qu, T.W. Yuan, W.Y. Wang, Y. Wu, Y.D. Li, Review of metal catalysts for oxygen reduction reaction: from nanoscale engineering to atomic design, Chem 5 (2019) 1486–1511.
[12] E. Proietti, F. Jaouen, M. Lefevre, N. Larouche, J. Tian, J. Herranz, J.P. Dodelet, Iron-based cathode catalyst with enhanced power density in polymer electrolyte membrane fuel cells, Nat. Commun. 2 (2011) 416.
[13] L. Zhao, Y. Zhang, L.B. Huang, X.Z. Liu, Q.H. Zhang, C. He, Z.Y. Wu, L.J. Zhang, J. Wu, W. Yang, L. Gu, J.S. Hu, L.J. Wan, Cascade anchoring strategy for general mass production of high-loading single-atomic metal-nitrogen catalysts, Nat. Commun. 10 (2019) 1278.
[14] J. Li, M.T. Sougrati, A. Zitolo, J.M. Ablett, I.C. Oğuz, T. Mineva, I. Matanovic, P. Atanassov, Y. Huang, I. Zenyuk, A. Di Cicco, K. Kumar, L. Dubau, F. Maillard, G. Dražić, F. Jaouen, Identification of durable and non-durable FeNx sites in

Fe–N–C materials for proton exchange membrane fuel cells, Nat. Catal. 4 (2020) 10–19.
[15] J. Li, C. Chen, L. Xu, Y. Zhang, W. Wei, E. Zhao, Y. Wu, C. Chen, Challenges and perspectives of single-atom-based catalysts for electrochemical reactions, JACS Au 3 (2023) 736–755.
[16] Y. Chen, S. Ji, C. Chen, Q. Peng, D. Wang, Y. Li, Single-atom catalysts: synthetic strategies and electrochemical applications, Joule 2 (2018) 1242–1264.
[17] Z. Yang, Y. Wang, M. Zhu, Z. Li, W. Chen, W. Wei, T. Yuan, Y. Qu, Q. Xu, C. Zhao, X. Wang, P. Li, Y. Li, Y. Wu, Y. Li, Boosting Oxygen Reduction Catalysis with Fe–N4 Sites Decorated Porous Carbons toward Fuel Cells, ACS Catal. 9 (2019) 2158–2163.
[18] H. Tian, A. Song, P. Zhang, K. Sun, J. Wang, B. Sun, Q. Fan, G. Shao, C. Chen, H. Liu, Y. Li, G. Wang, High durability of Fe-N-C single-atom catalysts with carbon vacancies toward the oxygen reduction reaction in alkaline media, Adv. Mater. 35 (2023), e2210714.
[19] X. Wan, Q. Liu, J. Liu, S. Liu, X. Liu, L. Zheng, J. Shang, R. Yu, J. Shui, Iron atom-cluster interactions increase activity and improve durability in Fe-N-C fuel cells, Nat. Commun. 13 (2022) 2963.
[20] Y. Chen, S. Ji, Y. Wang, J. Dong, W. Chen, Z. Li, R. Shen, L. Zheng, Z. Zhuang, D. Wang, Y. Li, Isolated single iron atoms anchored on N-doped porous carbon as an efficient electrocatalyst for the oxygen reduction reaction, Angew. Chem. Int Ed. Engl. 56 (2017) 6937–6941.
[21] X. Han, X. Ling, Y. Wang, T. Ma, C. Zhong, W. Hu, Y. Deng, Generation of nanoparticle, atomic-cluster, and single-atom cobalt catalysts from zeolitic imidazole frameworks by spatial isolation and their use in zinc-air batteries, Angew. Chem. Int. Ed. Engl 58 (2019) 5359–5364.
[22] L. Jiao, G. Wan, R. Zhang, H. Zhou, S.H. Yu, H.L. Jiang, From metal-organic frameworks to single-atom Fe implanted N-doped porous carbons: efficient oxygen reduction in both alkaline and acidic media, Angew. Chem. Int. Ed. Engl 57 (2018) 8525–8529.
[23] H. Zhang, S. Hwang, M. Wang, Z. Feng, S. Karakalos, L. Luo, Z. Qiao, X. Xie, C. Wang, D. Su, Y. Shao, G. Wu, Single atomic iron catalysts for oxygen reduction in acidic media: particle size control and thermal activation, J. Am. Chem. Soc. 139 (2017) 14143–14149.
[24] H. Huang, D. Yu, F. Hu, S.C. Huang, J. Song, H.Y. Chen, L.L. Li, S. Peng, Clusters induced electron redistribution to tune oxygen reduction activity of transition metal single-atom for metal-air batteries, Angew. Chem. Int. Ed. Engl 61 (2022), e202116068.
[25] S.N. Zhao, J.K. Li, R. Wang, J. Cai, S.Q. Zang, Electronically and geometrically modified single-atom Fe sites by adjacent Fe nanoparticles for enhanced oxygen reduction, Adv. Mater. 34 (2022), e2107291.
[26] X. Ao, W. Zhang, Z. Li, J.G. Li, L. Soule, X. Huang, W.H. Chiang, H.M. Chen, C. Wang, M. Liu, X.C. Zeng, Markedly Enhanced Oxygen Reduction Activity of Single-Atom Fe Catalysts via Integration with Fe Nanoclusters, ACS Nano 13 (2019) 11853–11862.
[27] X.Q. Wei, S.J. Song, W.W. Cai, X. Luo, L. Jiao, Q. Fang, X.S. Wang, N.N. Wu, Z. Luo, H.J. Wang, Z.H. Zhu, J. Li, L.R. Zheng, W.L. Gu, W.Y. Song, S.J. Guo, C.Z. Zhu, Tuning the spin state of Fe single atoms by Pd nanoclusters enables robust oxygen reduction with dissociative pathway, Chem 9 (2023) 181–197.
[28] T. He, Y. Chen, Q. Liu, B. Lu, X. Song, H. Liu, M. Liu, Y.N. Liu, Y. Zhang, X. Ouyang, S. Chen, Theory-guided regulation of FeN(4) spin state by neighboring Cu atoms for enhanced oxygen reduction electrocatalysis in flexible metal-air batteries, Angew. Chem. Int. Ed. Engl 61 (2022), e202201007.
[29] G. Yang, J. Zhu, P. Yuan, Y. Hu, G. Qu, B.A. Lu, X. Xue, H. Yin, W. Cheng, J. Cheng, W. Xu, J. Li, J. Hu, S. Mu, J.N. Zhang, Regulating Fe-spin state by atomically dispersed Mn-N in Fe-N-C catalysts with high oxygen reduction activity, Nat. Commun. 12 (2021) 1734.
[30] A. Han, W. Sun, X. Wan, D. Cai, X. Wang, F. Li, J. Shui, D. Wang, Construction of Co_4 Atomic Clusters to Enable Fe-N_4 Motifs with Highly Active and Durable Oxygen Reduction Performance, Angew. Chem. Int. Ed. Engl (2023), e202303185.
[31] A. Thomas, A. Fischer, F. Goettmann, M. Antonietti, J.-O. Müller, R. Schlögl, J. M. Carlsson, Graphitic carbon nitride materials: variation of structure and morphology and their use as metal-free catalysts, J. Mater. Chem. 18 (2008) 4893–4908.
[32] B.Y. Guan, L. Yu, X.W. Lou, A dual-metal–organic-framework derived electrocatalyst for oxygen reduction, Energy Environ. Sci. 9 (2016) 3092–3096.
[33] Y. Zhan, F. Xie, H. Zhang, Y. Jin, H. Meng, J. Chen, X. Sun, Highly dispersed nonprecious metal catalyst for oxygen reduction reaction in proton exchange membrane fuel cells, ACS Appl. Mater. Interfaces 12 (2020) 17481–17491.
[34] Y.L. Wu, J.L. Huang, Z.P. Lin, L.F. Li, G.F. Liang, Y.Q. Jin, G.J. Huang, H. Zhang, J. Chen, F.Y. Xie, Y.S. Jin, N. Wang, H. Meng, Fe-Nx doped carbon nanotube as a high efficient cathode catalyst for proton exchange membrane fuel cell, Chem. Eng. J. 423 (2021).
[35] P. Giannozzi, S. Baroni, N. Bonini, M. Calandra, R. Car, C. Cavazzoni, D. Ceresoli, G.L. Chiarotti, M. Cococcioni, I. Dabo, A. Dal Corso, S. de Gironcoli, S. Fabris, G. Fratesi, R. Gebauer, U. Gerstmann, C. Gougoussis, A. Kokalj, M. Lazzeri, L. Martin-Samos, N. Marzari, F. Mauri, R. Mazzarello, S. Paolini, A. Pasquarello, L. Paulatto, C. Sbraccia, S. Scandolo, G. Sclauzero, A.P. Seitsonen, A. Smogunov, P. Umari, R.M. Wentzcovitch, QUANTUM ESPRESSO: a modular and open-source software project for quantum simulations of materials, J. Phys. Condens. Matter 21 (2009), 395502.
[36] P.J. Hasnip, C.J. Pickard, Electronic energy minimisation with ultrasoft pseudopotentials, Comput. Phys. Commun. 174 (2006) 24–29.
[37] J.P. Perdew, K. Burke, M. Ernzerhof, Generalized gradient approximation made simple, Phys. Rev. Lett. 77 (1996) 3865–3868.
[38] J.P. Perdew, J.A. Chevary, S.H. Vosko, K.A. Jackson, M.R. Pederson, D.J. Singh, C. Fiolhais, Atoms, molecules, solids, and surfaces: Applications of the generalized gradient approximation for exchange and correlation, Phys. Rev. B Condens. Matter 46 (1992) 6671–6687.
[39] J.K. Nørskov, J. Rossmeisl, A. Logadottir, L. Lindqvist, J.R. Kitchin, T. Bligaard, H. Jónsson, Origin of the overpotential for oxygen reduction at a fuel-cell cathode, J. Phys. Chem. B 108 (2004) 17886–17892.
[40] X.L. Zhao, X.X. Yang, M.Y. Wang, S. Hwang, S. Karakalos, M.J. Chen, Z. Qiao, L. Wang, B. Liu, Q. Ma, D.A. Cullen, D. Su, H.P. Yang, H.Y. Zang, Z.X. Feng, G. Wu, Single-iron site catalysts with self-assembled dual-size architecture and hierarchical porosity for proton-exchange membrane fuel cells, Appl. Catal. B-Environ 279 (2020), 119400.
[41] X. Wan, X. Liu, Y. Li, R. Yu, L. Zheng, W. Yan, H. Wang, M. Xu, J. Shui, Fe–N–C electrocatalyst with dense active sites and efficient mass transport for high-performance proton exchange membrane fuel cells, Nat. Catal. 2 (2019) 259–268.
[42] C.C. Hou, L. Zou, L. Sun, K. Zhang, Z. Liu, Y. Li, C. Li, R. Zou, J. Yu, Q. Xu, Single-atom iron catalysts on overhang-eave carbon cages for high-performance oxygen reduction reaction, Angew. Chem. Int. Ed. Engl 59 (2020) 7384–7389.
[43] M.J. Chen, X. Li, F. Yang, B.Y. Li, T. Stracensky, S. Karakalos, S. Mukerjee, Q.Y. Jia, D. Su, G.F. Wang, G. Wu, H. Xu, Atomically Dispersed MnN4 Catalysts via Environmentally Benign Aqueous Synthesis for Oxygen Reduction: Mechanistic Understanding of Activity and Stability Improvements, ACS Catal. 10 (2020) 10523–10534.
[44] D. Zhang, W. Chen, Z. Li, Y. Chen, L. Zheng, Y. Gong, Q. Li, R. Shen, Y. Han, W. C. Cheong, L. Gu, Y. Li, Isolated Fe and Co dual active sites on nitrogen-doped carbon for a highly efficient oxygen reduction reaction, Chem. Commun 54 (2018) 4274–4277.
[45] Y. Zhao, P.V. Kumar, X. Tan, X. Lu, X. Zhu, J. Jiang, J. Pan, S. Xi, H.Y. Yang, Z. Ma, T. Wan, D. Chu, W. Jiang, S.C. Smith, R. Amal, Z. Han, X. Lu, Modulating Pt-O-Pt atomic clusters with isolated cobalt atoms for enhanced hydrogen evolution catalysis, Nat. Commun. 13 (2022) 2430.
[46] Q. Cheng, C. Hu, G. Wang, Z. Zou, H. Yang, L. Dai, Carbon-defect-driven electroless deposition of Pt atomic clusters for highly efficient hydrogen evolution, J. Am. Chem. Soc. 142 (2020) 5594–5601.
[47] J.-C. Li, F. Xiao, H. Zhong, T. Li, M. Xu, L. Ma, M. Cheng, D. Liu, S. Feng, Q. Shi, H.-M. Cheng, C. Liu, D. Du, S.P. Beckman, X. Pan, Y. Lin, M. Shao, Secondary-atom-assisted synthesis of single iron atoms anchored on N-doped carbon nanowires for oxygen reduction reaction, ACS Catal. 9 (2019) 5929–5934.
[48] Y. He, H. Guo, S. Hwang, X. Yang, Z. He, J. Braaten, S. Karakalos, W. Shan, M. Wang, H. Zhou, Z. Feng, K.L. More, G. Wang, D. Su, D.A. Cullen, L. Fei, S. Litster, G. Wu, Single Cobalt Sites Dispersed in Hierarchically Porous Nanofiber Networks for Durable and High-Power PGM-Free Cathodes in Fuel Cells, Adv. Mater. 32 (2020), e2003577.
[49] S.H. Lee, J. Kim, D.Y. Chung, J.M. Yoo, H.S. Lee, M.J. Kim, B.S. Mun, S.G. Kwon, Y. E. Sung, T. Hyeon, Design principle of Fe-N-C electrocatalysts: how to optimize multimodal porous structures? J. Am. Chem. Soc. 141 (2019) 2035–2045.
[50] J. Pampel, T.-P. Fellinger, Opening of bottleneck pores for the improvement of nitrogen doped carbon electrocatalysts, Adv. Energy Mater. 6 (2016), 1502389.
[51] Y. Chen, T. He, Q. Liu, Y. Hu, H. Gu, L. Deng, H. Liu, Y. Liu, Y.-N. Liu, Y. Zhang, S. Chen, X. Ouyang, Highly durable iron single-atom catalysts for low-temperature zinc-air batteries by electronic regulation of adjacent iron nanoclusters, Appl. Catal. B: Environ 323 (2023), 122163.
[52] S. Liu, B. Zhang, Y. Cao, H. Wang, Y. Zhang, S. Zhang, Y. Li, H. Gong, S. Liu, Z. Yang, J. Sun, Understanding the Effect of Nickel Doping in Cobalt Spinel Oxides on Regulating Spin State to Promote the Performance of the Oxygen Reduction Reaction and Zinc–Air Batteries, ACS Energy Lett. 8 (2022) 159–168.
[53] L. Sun, M. Lu, Z. Yang, Z. Yu, X. Su, Y.Q. Lan, L. Chen, Nickel glyoximate based metal-covalent organic frameworks for efficient photocatalytic hydrogen evolution, Angew. Chem. Int. Ed. Engl 61 (2022), e202204326.
[54] Z. Zhuang, L. Xia, J. Huang, P. Zhu, Y. Li, C. Ye, M. Xia, R. Yu, Z. Lang, J. Zhu, L. Zheng, Y. Wang, T. Zhai, Y. Zhao, S. Wei, J. Li, D. Wang, Y. Li, Continuous modulation of electrocatalytic oxygen reduction activities of single-atom catalysts through p-n junction rectification, Angew. Chem. Int. Ed. Engl 62 (2023), e202212335.
[55] N. Ramaswamy, U. Tylus, Q. Jia, S. Mukerjee, Activity descriptor identification for oxygen reduction on nonprecious electrocatalysts: linking surface science to coordination chemistry, J. Am. Chem. Soc. 135 (2013) 15443–15449.
[56] A. Gaur, N. Nitin Nair, B.D. Shrivastava, B.K. Das, M. Chakrabortty, S.N. Jha, D. Bhattacharyya, Study of distorted octahedral structure in 3d transition metal complexes using XAFS, Chem. Phys. Lett. 692 (2018) 382–387.
[57] R.H. Sanchez, T.A. Betley, Thermally persistent high-spin ground states in octahedral iron clusters, J. Am. Chem. Soc. 140 (2018) 16792–16806.
[58] N. Thi Kim Nguyen, M. Dubernet, Y. Matsui, M. Wilmet, N. Shirahata, G. Rydzek, N. Dumait, M. Amela-Cortes, A. Renaud, S. Cordier, Y. Molard, F. Grasset, T. Uchikoshi, Transparent functional nanocomposite films based on octahedral metal clusters: synthesis by electrophoretic deposition process and characterization, R. Soc. Open Sci. 6 (2019), 181647.
[59] Z.W. Seh, J. Kibsgaard, C.F. Dickens, I. Chorkendorff, J.K. Norskov, T.F. Jaramillo, Combining theory and experiment in electrocatalysis: Insights into materials design, Science 355 (2017).

[60] H. Wang, J.K. Keum, A. Hiltner, E. Baer, B. Freeman, A. Rozanski, A. Galeski, Confined crystallization of polyethylene oxide in nanolayer assemblies, Science 323 (2009) 757–760.
[61] Y. Xie, X. Chen, K. Sun, J. Zhang, W.H. Lai, H. Liu, G. Wang, Direct oxygen-oxygen cleavage through optimizing interatomic distances in dual single-atom electrocatalysts for efficient oxygen reduction reaction, Angew. Chem. Int. Ed. Engl 62 (2023), e202301833.
[62] Z. Wang, X. Jin, R. Xu, Z. Yang, S. Ma, T. Yan, C. Zhu, J. Fang, Y. Liu, S.J. Hwang, Z. Pan, H.J. Fan, Cooperation between dual metal atoms and nanoclusters enhances activity and stability for oxygen reduction and evolution, ACS Nano 17 (2023) 8622–8633.